Journal of Inorganic and Organometallic Polymers and Materials (2021) 31:3677–3685
https://doi.org/10.1007/s10904-021-02037-7

Facile Synthesis of Polypyrrole/Reduced Graphene Oxide Composite Hydrogel for Cr(VI) Removal

Song Gao[1,2] · Zhichang Liu[1] · Qunshan Yan[1] · Pei Wei[1] · Yang Li[2] · Jiayou Ji[2] · Liang Li[2]

Received: 2 February 2021 / Accepted: 22 May 2021 / Published online: 31 May 2021

Abstract

Polymeric-inorganic composites are promising for the efficient treatment of contaminated water. In this work, the recyclable composite hydrogel with three-dimensional network composed of polypyrrole and reduced graphene oxide are synthesized through a hydrothermal process using polypyrrole nanotubes and graphene oxide as the precursors. Due to the synergic effect between graphene nanosheets and polypyrrole nanotubes, the composite hydrogel exhibits excellent removal capability of 395 mg g^{-1} for Cr(VI) removal through the simultaneous adsorption and chemical reduction. The adsorption equilibrium isotherm is well fitted with the Langmuir adsorption model. The result of adsorption kinetics is simulated by the pseudo-second-order model. The composite hydrogel still possesses Cr(VI) removal capacity without a significant decrease in the presence of coexisting cations. Moreover, because of the stable network in the composite hydrogel, it can be easily separated from the contaminated water after adsorption and can be regenerated and reused efficiency after six adsorption-desorption cycles. Thus, polypyrrole/reduced graphene oxide composite hydrogel provides a potential platform as a cost-effective material for Cr(VI) removal applications.

Graphic Abstract

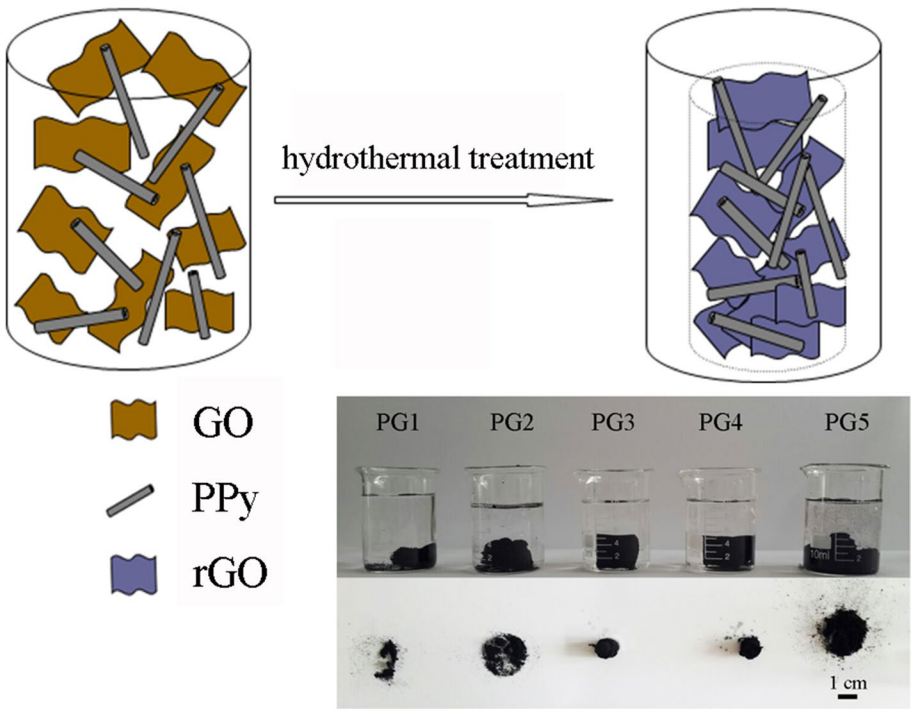

Extended author information available on the last page of the article

Keywords Composites · Polypyrrole · Graphene · Hydrogel · Cr(VI) removal

1 Introduction

The rapid development of industry and social activities inevitably results in the accidents of water pollution. The contaminated water is not only harmful to the environment and human health, but also brings about the tremendous economic loss [1–5]. Heavy metal and organic compounds are the main kinds of contaminants in the wastewater. Although most metals at a trace level are definitely necessary for human, non-biodegradable metals will have adverse effects on living organism at high concentration. Among them, chromium (Cr) as the second most groundwater contaminant is widely used in electroplating, tanning, and other industries [6]. Cr(VI) and Cr(III) are the primary Cr ion states in aqueous solution. The former is more toxic and carcinogenic [7]. Therefore, the development of low-cost and effective techniques for the removal of Cr(VI) is of great interest in wastewater treatment.

Many technologies, such as filtration, reverse osmosis, adsorption, chemical oxidation, coagulation, and bio-degradation, have been developed for the elimination of pollutants and minimized the adverse effect of water pollution. Compared with other technologies for water treatment, adsorption is considered to possess the feasibility, low-cost and environmentally friendly characteristics, and high removal ability. Several adsorbent materials with porous structure or functional surface, such as zeolite, metal oxide and activated carbon, have been extensively applied for Cr(VI) removal [8–10]. Since the discovery of conducting polypyrrole (PPy), it has been considered as one of the most promising materials owing to easy preparation, tunable chemical and electrochemical performance, biocompatibility [11–13]. Moreover, the removal of heavy metal ions from the contaminated water using PPy with the property of ion exchange has been reported in the previous studies [14–16]. Graphene as a kind of thin two-dimensional carbon nanomaterial has attracted considerable attention for the treatment of contaminated water [17–20]. However, graphene easily tends to agglomerate due to its large surface area, decreasing its adsorption efficiency. The anchoring of other nanomaterials on the surface of graphene nanosheets in the composites may prevent graphene nanosheets from severe restacking, and nanomaterials themselves. It leads to the increase of the specific surface area in the obtained composites, which is beneficial for the adsorption performance.

Recently, polymeric-inorganic composites due to their hierarchical structures and distinctive integrated properties have been widely used in various fields. Chen et al. prepared the core-shell nanocomposites via the chemical polymerization of PPy on the surface of attapulgite for Cr(VI) removal [21]. Yao et al. anchored Fe_3O_4 and polypyrrole nanoparticles on graphene nanosheets via two steps to construct the magnetic hybrid nanocomposites with hierarchical structure [22]. The nanocomposite adsorbent powders were not easily removed after adsorption and unsuitable for cycle use though they can remove heavy metal ions fast [23]. In spite of the simplified procedure in separation, magnetic nanocomposites exhibit unsatisfactory removal ability due to the disadvantages of aggregation [24]. Taking the requirement of advanced adsorbents into consideration, it is imperative to design and prepare an integrated architecture, in which the advantages of each component can be comprehensively utilized, to act as excellent adsorbents for Cr(VI) removal. Most of the composite adsorbents in the shape of powders were not easily removed after adsorption and unsuitable for cycle use though they possessed excellent Cr(IV) removal ability. Therefore, the development of advanced polymeric-inorganic adsorbents with high adsorption capacity and facile separation ability is still urgent through the design of an integrated architecture, in which the interconnection of each component can be realized and the merit of each component can be preserved.

In our previous report, PPy nanotubes were successfully synthesized through the soft template of cation and methyl orange [25]. Herein, a facile hydrothermal synthetic process is presented for the preparation of the three-dimensional macroscopic PPy/reduced graphene oxide (PPy/rGO) composite hydrogels assembled by one-dimensional PPy nanotubes and two-dimensional graphene nanosheets. The optimized feed ratio of PPy and graphene oxide (GO) contributes to the formation of stable macroscopic structure. The adsorption isotherms and adsorption kinetics of Cr(VI) on PPy/reduced graphene oxide composite hydrogel are estimated with Freundlich and Langmuir isotherm models as well as the pseudo-second order. The synergistic interactions between PPy and graphene in the stable composite hydrogel enable the efficient removal of Cr(VI), easy separation after adsorption as well as recyclability.

2 Experimental

2.1 Synthesis of PPy/Reduced Graphene Oxide Composite Hydrogel

PPy nanotubes and GO were synthesized according to the previous reports, respectively [25, 26]. The predetermined PPy nanotubes were dispersed in 10 mL aqueous solution containing 2 mg mL^{-1} GO and ultra-sonicated for 30 min at room temperature. Then, the above mixture was transferred

to a stainless-steel Teflon-lined autoclave and heated at 180 °C for 3 h. The obtained products were taken out and washed with deionized water and ethanol several times. The composite products prepared in the cases of PPy amounts of 20, 25, 30, 50, 100 mg were designated as PG1, PG2, PG3, PG4, and PG5, respectively.

2.2 Characterization

The morphology of the products was observed by scanning electron microscope (SEM, JSM-5510LV, JEOL Co.). X-ray diffraction (XRD) patterns were analyzed on PHILIPS PW 3710 diffractometer using Cu Ka radiation at room temperature. Brunauer-Emmett-Teller (BET) surface area of the product was measured on a Micromeritics ASAP 2010 M instrument. X-ray photoelectron spectroscopy (XPS) was carried out using a spectrometer (ESCALB MK-II, VG Co., England) under a base pressure of 1×10^{-9} Torr using Mg Kα monochromatic X-ray source at 1253.6 eV.

For the Cr(VI) adsorption experiments, 8 mg of the product was added into a flask containing 40 mL of Cr(VI) solution (120 mg L^{-1}) at pH 2.0. After stirring for a certain time, an amount of the suspension was taken out. An ultraviolet spectrophotometer (SHIMADZU UV-2501) was employed to determine the concentration of Cr(VI) ions. The adsorption capacity of Cr(VI) ions was calculated by the following equation:

$$q_t = (C_o - C_t)V/m \quad (1)$$

where q_t (mg g^{-1}) was the adsorption capacity at a certain time, C_0 (mg L^{-1}) was the initial concentration and C_t (mg L^{-1}) was the concentration at a certain time. V (L) was the solution volume, m (g) was the adsorbent mass.

3 Results and Discussion

Figure 1 showed a schematic of the hydrothermal synthesis process for PPy/rGO composite hydrogel when PPy nanotubes and GO were used as the precursors. It was impossible to disperse PPy nanotubes uniformly in water and the precipitation due to the aggregation of PPy nanotubes inevitably happened even after long time sonication. It is well known that the oxygen-containing groups such as carbonyl and carboxyl groups endow GO with hydrophilicity. The previous reports have demonstrated that GO could be used as an effective dispersant like the surfactant to realize the dispersion of carbon nanotubes or porphyrin assembly in solution [27, 28]. Therefore, PPy was effectively dispersed in the presence of GO with the aid of ultrasonication in this work. As shown in Fig. 1, GO nanosheets was able to adsorb PPy via π-π interaction between the aromatic structure of GO and the conjugated chain of PPy, resulting in the formation of a stable mixture suspension. Accompanied with the reduction and self-assembly of GO nanosheets during the hydrothermal process, PPy nanotubes dispersed in GO aqueous solution were embedded into the graphene network to obtain a three-dimensional composite hydrogel. The feed ratio of PPy and GO on the formation of composite hydrogel was further studied. After hydrothermal treatment, the black suspension disappeared and a black product emerged from the water for all of the cases. However, it was worth noting that when the mass ratio of PPy and GO was below 1.5, the as-prepared products were very fragile. Only the powders were obtained after freeze drying for PG1 and PG2, as show in Fig. 2. When the mass ratio of PPy and GO was 1.5, an entire PG3 hydrogel was prepared and a self-standing block was kept after freeze-drying. Moreover, the freeze-dried PG3 hydrogel could support a counterweight, which was about more than 1000 times of its own weight, as shown in Fig. 2b. It indicated that a stable hydrogel was prepared in the case of the increased amount of PPy nanotubes, which might be related to the efficient network assembled by PPy

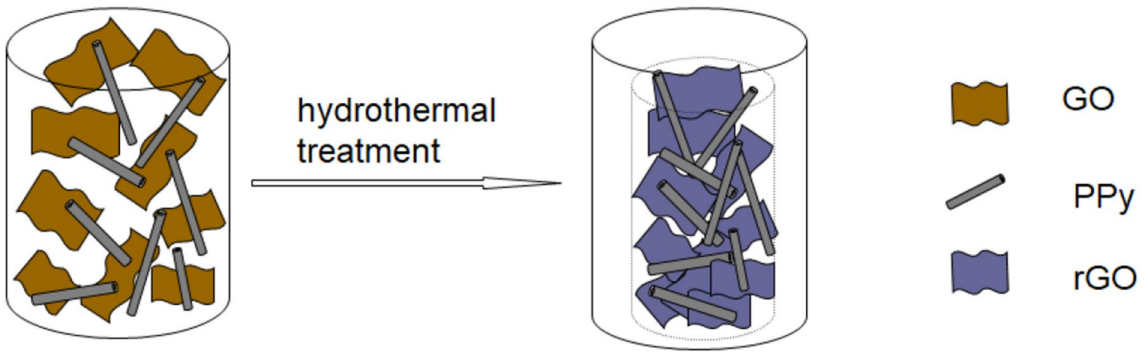

Fig. 1 Schematic of the synthesis of PPy/rGO composite hydrogels

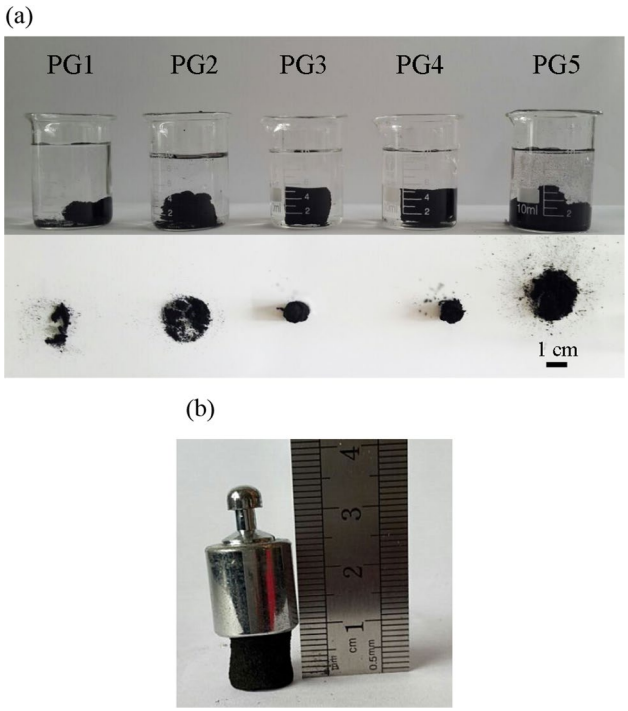

Fig. 2 **a** Photos of the products (above) and after freeze-drying from top-view (below). **b** Photo of the freeze-dried PG3 supporting a counterweight

nanotubes and graphene nanosheets. In our previous work, the static oxidation polymerization of pyrrole monomer in GO aqueous solution at room temperature resulted in the formation of three-dimensional PPy/GO composite hydrogels by one-step self-assembly method [29]. This PPy/GO composite hydrogel was very soft, just like playdough. However, in this work, PPy/rGO composite hydrogel prepared by the hydrothermal treatment could support a counterweight. Therefore, the hydrothermal treatment was essential for the preparation of the composite hydrogel with good mechanical property. The mass ratio of PPy and GO was further increased in this work. It was unexpected that when the mass ratio of PPy and GO reached and exceeded 2.5, the freeze-dried hydrogels gradually lost their self-standing feature although it seemed that the as-prepared products supported themselves after hydrothermal process. Therefore, more or less PPy nanotubes were not beneficial for the formation of stable hydrogel. When less PPy nanotubes was present, the network between PPy nanotubes and GO nanosheets was weak, resulting in the unstable hydrogel. On the other hand, it was uneasy for more PPy to disperse in GO aqueous solution, which was adverse for the preparation of the composite hydrogel.

The morphologies of the freeze-dried GO, PPy, PG3 composite hydrogel were shown in Fig. 3. Several wrinkled and smooth layers could be observed in SEM image of pure GO. One-dimensional nanoblocks with a diameter of about 100–200 nm and a length of several micrometers could be seen in SEM image of PPy, which was in agreement with our

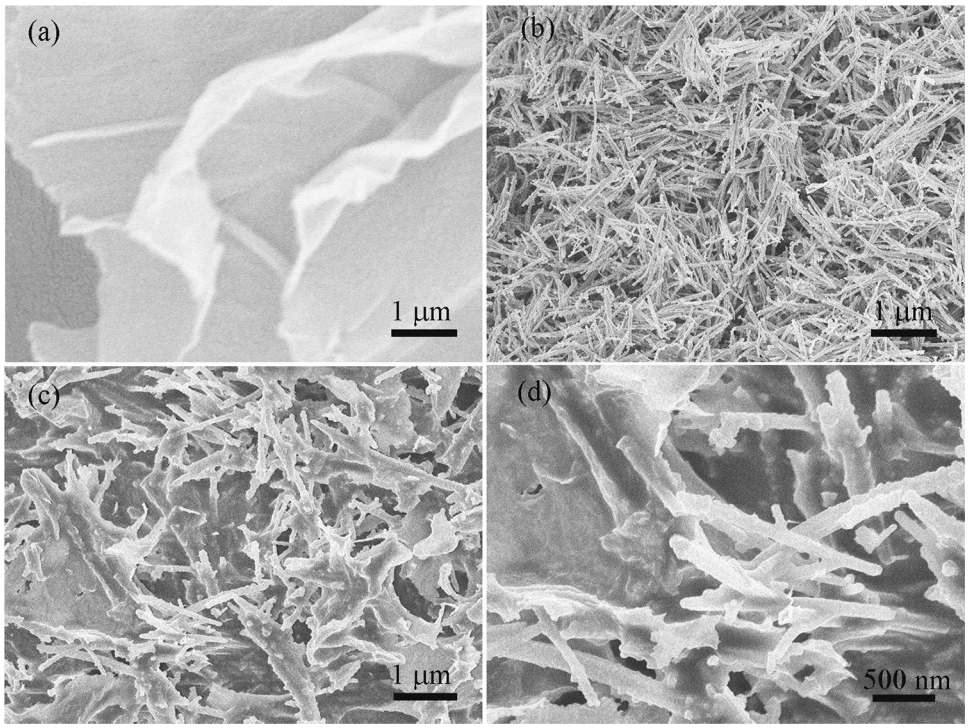

Fig. 3 SEM images of **a** GO, **b** PPy, and **c**, **d** PG3

previous report [25]. For PG3 composite hydrogel, there was a multilayered hierarchical porous network structure, where one-dimensional PPy nanotubes were tightly intertwined among graphene layers. The magnified image in Fig. 3d further revealed that one-dimensional PPy close located to the edges of graphene or link the adjacent individual graphene nanosheets, which was in favor of the formation of the well-defined and interconnected PPy/rGO composite hydrogel driven by several interactions including π-π conjugation and physical entanglement of PPy and graphene.

XRD patterns of GO, rGO, PPy, and the composites were given in Fig. 4 A and Fig. S1. The characteristic peak at about 2θ = 11° was attributed to the diffraction plane (001) reflection of GO [30]. For rGO, the diffraction peak (001) disappeared and the diffraction peak (002) at 2q = 24.2° appeared, indicating the disordered restacking of graphene nanosheets. The weak around a 2θ value of 20°–30° was characteristic of the amorphous PPy macromolecules [31]. Interestingly, the composite of PG3 possessed the similar XRD pattern without the appearance of peak for GO, indicating the formation of rGO in the composite hydrogel through the reduction of GO during the hydrothermal treatment. Raman spectra of GO, rGO and PG3 were shown in Fig. 4B. Two typical peaks at 1330 cm^{-1} (D band) and 1585 cm^{-1} (G band) were observed for GO and rGO [32]. For PG3, the two bands in the range of 1300–1590 cm^{-1} owing to C = C backbone stretching and ring-stretching mode of PPy [33] were overlapped by the D and G bands of graphene. However, it also contained a series of weak peaks at about 900–1100 cm^{-1}, belonging to C-H in-plane deformation of pyrrole ring. The broad D band with weak intensity in PG3 could be ascribed to the interaction between PPy and graphene nanosheets [33, 34]. Moreover, the intensity ratio I_D/I_G of GO (0.92) was lower than that of PG3 (1.1) and rGO (1.3), which indicated that the reduction of GO into rGO during the hydrothermal assembly process [35]. XPS spectra of GO and PG3 were presented in Fig. 4c. After the hydrothermal process, nitrogen atoms have been successfully incorporated through the combination of PPy and graphene. Moreover, the presence of a small peak belonging to sulfur might be attributed to the residue of methyl orange, which was doped into PPy during the synthesis of PPy nanotubes. The BET specific surface area of the freeze-dried PG3 composite investigated by nitrogen isothermal adsorption was about 94.3 $m^2\ g^{-1}$, which was larger than those of PPy nanotube (22.5 $m^2\ g^{-1}$) and graphene aerogel (68.3 $m^2\ g^{-1}$). It is expected that the combined components of PPy and graphene, together with the three-dimensional network structures with high specific surface area in the PG3 composite hydrogel ensure its potential application in wastewater treatment.

The feasibility of PG3 as an efficient adsorbent for Cr(VI) removal was explored. The adsorption capacity of Cr(VI) for

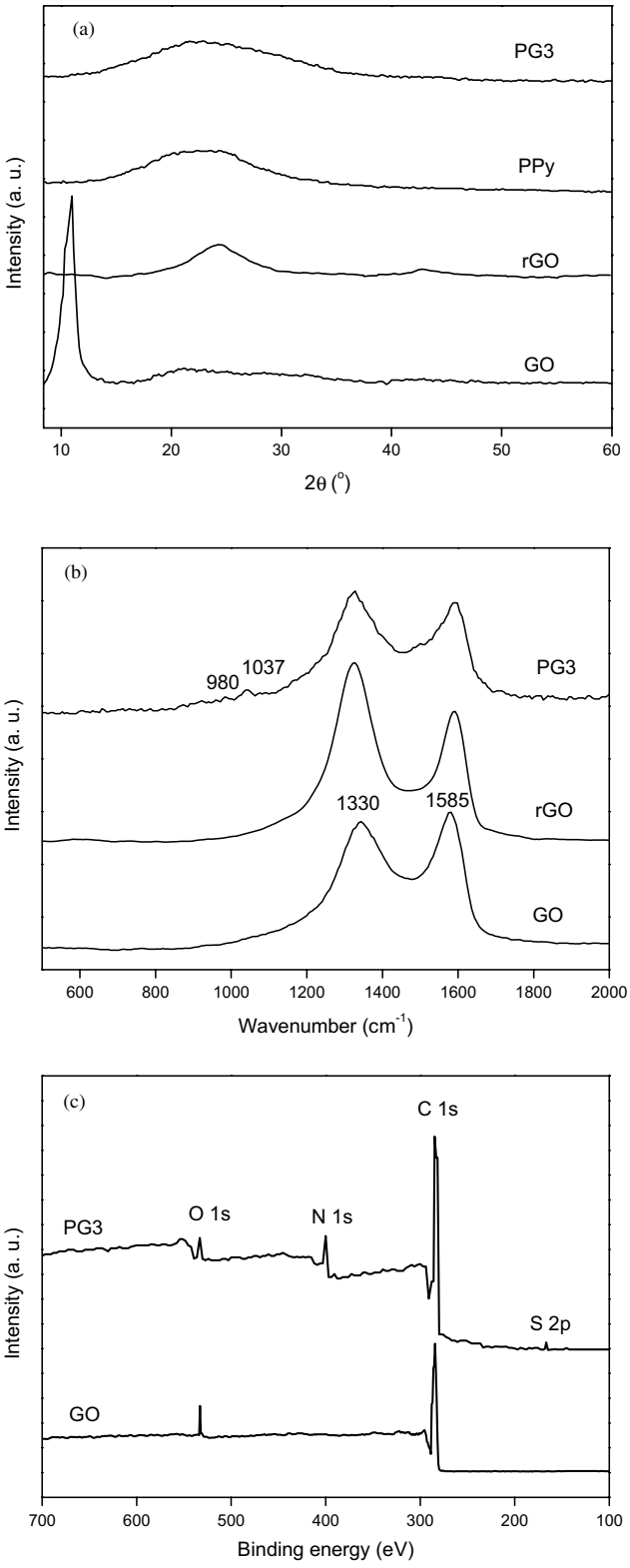

Fig. 4 **a** XRD patterns of GO, rGO, PPy, and PG3. **b** Raman spectra of GO, rGO and PG3. **c** XPS spectra of GO and PG3

PPy and PG3 with the adsorption time was first compared. Apparently, the adsorption capacity of Cr(VI) for PG3 was much larger than that of PPy, as shown in Fig. 5a. Moreover, it was observed that adsorption capacity increased rapidly in the initial stage and reached 50 % of the maximum adsorption in about 60 and 90 min for PPy and PG3, respectively. Then it continued to increase slowly until an adsorption equilibrium arrived. These phenomena demonstrated that the initial Cr(VI) adsorption mainly occurred on the surface of PPy and PG3, and it need more time for PG3 to gradually spread into the inner part of the composite hydrogel in contrast with the powder PPy. Pseudo-second-order kinetic model for adsorption of Cr(VI) was used to evaluate the adsorption properties of PPy and PG3. The adsorption results were calculated by the following pseudo-second-order equation [36]:

$$\frac{t}{q_t} = \frac{1}{k_2 q_e^2} + \frac{t}{q_e} \tag{2}$$

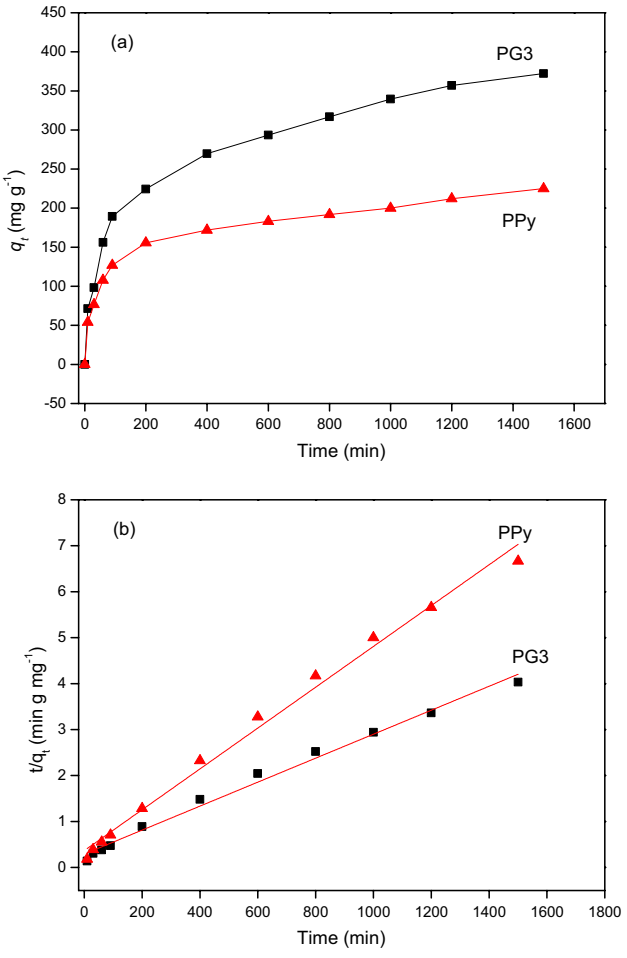

Fig. 5 **a** Adsorption capacity versus time of PPy and PG3. **b** Pseudo-second-order kinetic model for adsorption of Cr(VI) by PPy and PG3

where q_e and q_t were the equilibrium adsorption capacity and adsorption capacity at a certain time, respectively, and k_2 was the pseudo-second-order rate constant. As shown in Fig. 5b, the linear behaviors between time and t/q_t for PPy and PG3 confirmed the good simulation by pseudo-second-order model. The equilibrium Cr(VI) adsorption capacities were calculated to be 383 and 225 mg g^{-1} for PG3 and PPy, respectively. These results indicated that PPG3 exhibited much better Cr(VI) adsorption performance than PPy.

Langmuir isotherm model and Freundlich isotherm model, expressed in the following Eqs. 3 and 4, were further used to simulate the adsorption thermodynamics for PG3, respectively [37].

$$\frac{C_e}{q_e} = \frac{1}{k_L q_m} + \frac{C_e}{q_m} \tag{3}$$

$$\lg q_e = \lg k_F + \frac{1}{n} \lg C_e \tag{4}$$

where C_e was the equilibrium concentration, q_m was the maximum adsorption capacity, and k_L was Langmuir adsorption constant, k_F and n were Freundlich constants relevant to the adsorption capacity and adsorption intensity, respectively (Fig. 6). Based on the above equations, the correlation coefficients were simulated to be 0.995 and 0.982 for Langmuir and Freundlich model, respectively, which suggested that the adsorption results were well fitted with Langmuir model. The maximum Cr(VI) adsorption capacity for PG3 was 395 mg g^{-1}, which was close to the experimental result shown in Fig. 5. The adsorption capacity calculated from Langmuir model was compared with other PPy-based adsorbents reported previously. As shown in Table 1, the adsorption capacity of PG3 was higher than or comparable to those of PPy-based composite and activated carbon adsorbents. Moreover, this composite hydrogel could be conveniently separated from the wastewater because of its stable monolith.

Other cations, such as alkaline metal ions, generally co-exist in the wastewater containing Cr(VI) ions. The influence of Na^+, K^+, Mg^{2+}, or Ca^{2+} ions on the Cr(VI) removal for PG3 was given in Fig. 7a. The adsorption capacity of Cr(VI) just decreased about 10 % in the solutions containing other metals likely owing to the co-existing ion effect. It suggested that the selective adsorption of Cr(VI) ions was main for the prepared PG3 composite hydrogel in favor of its potential practical application. Furthermore, the stability and regeneration property of the prepared PG3 composite hydrogel for economic consideration were investigated. PG3 after adsorption was immersed in 0.1 mol L^{-1} NaOH solution followed by in 0.5 mol L^{-1} HCl solution [45]. Figure 7b presented the reusability and regeneration performance of PG3 after

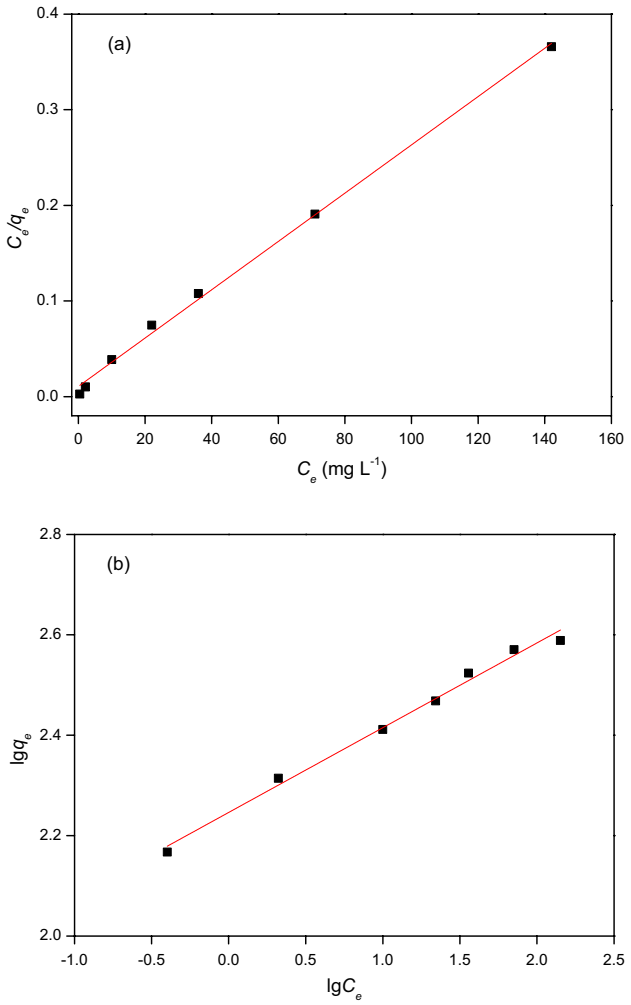

Fig. 6 Fit of equilibrium data to **a** Langmuir isotherm model and **b** Freundlich isotherm model obtained for PG3

Table 1 Comparison of removal capacity of PG3 with other adsorbents

Adsorbents	q_m (mg g^{-1})	pH	Ref.
PPy/attapulgite nanocomposite	49	3.0	[21]
graphene@Fe_3O_4@PPy microsphere	348	2.0	[22]
nanofibers of PPy-polyaniline	227	2.0	[38]
PPy porous nanoclusters	180	5.0	[39]
PPy-chitosan nanocomposite	79	2.0	[40]
PPy/m-phenylediamine/Fe_3O_4 composite	555	2.0	[41]
Polypyrrole/hollow silica particles	322	2.0	[42]
activated carbon from cassava peels	166	3.0	[43]
activated carbon from sugar beet residue	164	4.5	[44]
PG3	395	2.0	This work

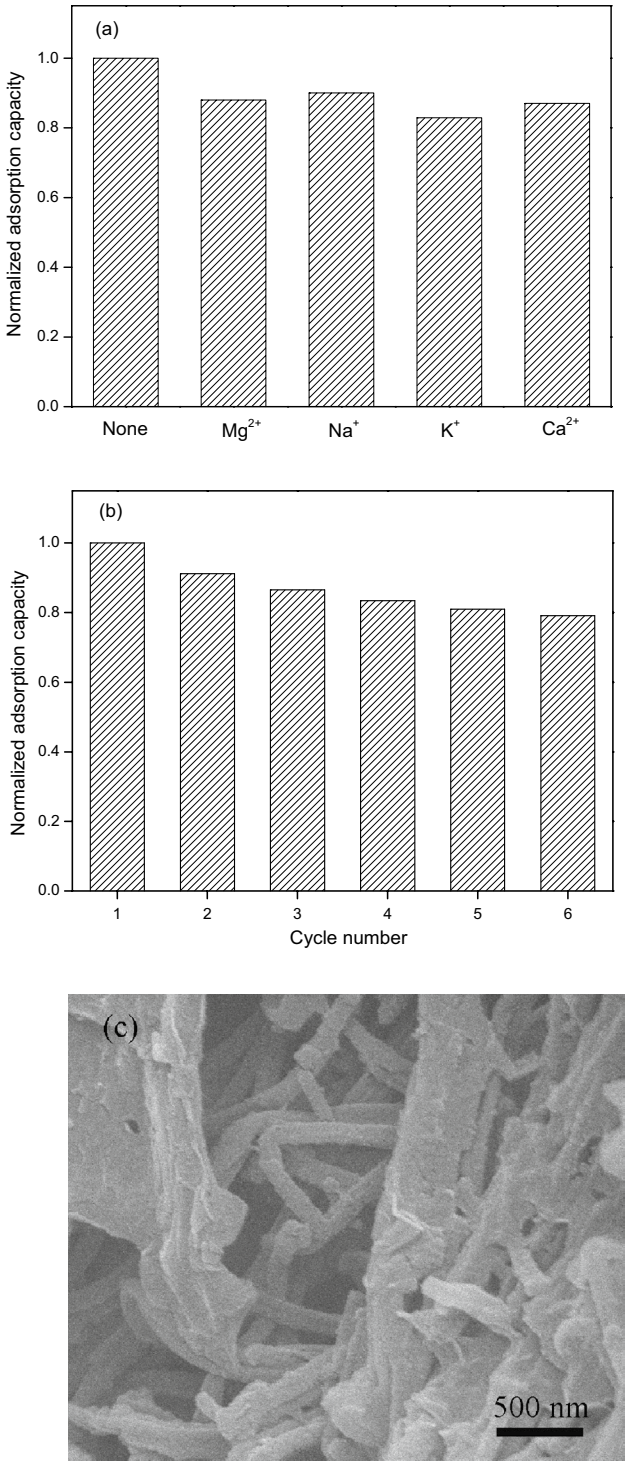

Fig. 7 **a** Effect of co-existing cations on Cr(VI) removal. **b** adsorption cycles of Cr(VI) removal for PG3. **c** The morphology of PG3 after six cycles

six adsorption-desorption cycles. It showed that about 79.1 % of the Cr(VI) removal ability was kept, indicating that PG3 can be used as a recyclable absorbent for Cr(VI) ions. The used PG3 still presented as the one-dimensional

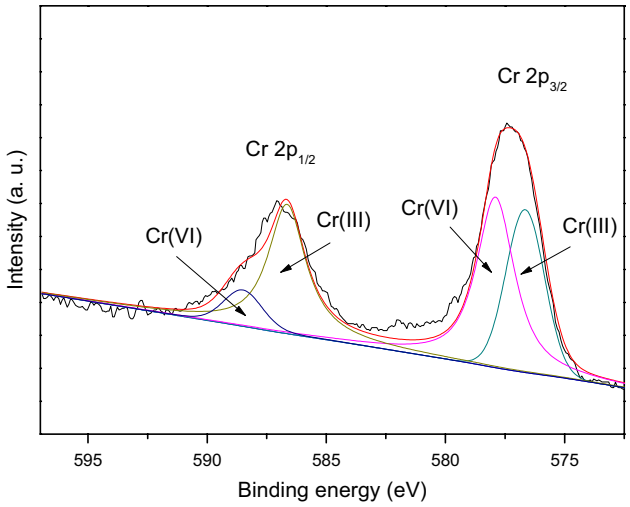

Fig. 8 XPS high-resolution spectrum of Cr 2p after Cr(VI) adsorption

nanoblocks embedded into the graphene network, and no obvious change was observed in the morphology (Fig. 7c). Moreover, after six cycles of the adsorption-desorption process, PG3 could still be separated easily because of its stable architecture.

XPS spectrum of these composites after adsorption was further recorded to investigate the mechanism of efficient removal of Cr (VI) by PG3. As shown in Fig. 8, two energy bands around 577.1 and 587 eV belonged to Cr $2p_{3/2}$ and Cr $2p_{1/2}$, respectively. It was worthy noting that Cr $2p_{3/2}$ peak could be divided into two valence states at 576.6 and 578 eV, which are in agreement with Cr(III) and Cr(VI), respectively. Meanwhile, Cr $2p_{1/2}$ peak could also be separated into two valence states at 586.7 and 588.5 eV, which are in accordance with Cr(III) and Cr(VI), respectively [46]. Furthermore, the molar ratio of Cr(VI) and Cr(III) was calculated to be about 42 and 58 %, respectively. Therefore, both Cr(III) and Cr(VI) existed on the PG3 composite hydrogel after Cr(VI) removal. The appearance of Cr(III) could be ascribed to the reduction of some adsorbed Cr(VI) ions by the electron-rich groups of PPy macromolecules during the adsorption process [47]. When Cr(VI) ions appeared as $HCrO_4^-$ at pH 2, leading to electrostatically mediated Cr removal. First, the enrichment of Cr(VI) on the composite occurred through electrostatic interaction and ion exchange because PPy was positively charged in the acid solution. Then, the portion loaded by PG3 took part in a redox reaction. The redox reaction between $HCrO_4^-$ and PPy happened due to the higher redox potential of $HCrO_4^-$ in the acidic condition. Therefore, the composite hydrogel and Cr(VI) underwent electrostatic interaction, ion exchange, and redox reaction for the removal of chromium.

4 Conclusions

The PPy/rGO composite hydrogels were successfully fabricated via anchoring one-dimensional polypyrrole nanotubes on two-dimensional graphene nanosheets through hydrothermal treatment. The composite hydrogel exhibited high removal ability of Cr(VI) owing to the three-dimensional network and the synergistic interaction between PPy and rGO. The adsorption kinetics and isotherms followed the pseudo-second order kinetics and Langmuir adsorption isotherm model, respectively. The composite hydrogel retained about 79.1 % of the removal performance after six successive cycles. Therefore, the combination of excellent adsorption efficiency, reusability, facile separating process ensured a bright future of PPy/rGO composite hydrogel in the sustainable application of wastewater treatment.

Supplementary Information The online version contains supplementary material available at https://doi.org/10.1007/s10904-021-02037-7.

Author Contributions SG: Experiment, Writing-original draft; ZL: Analysis; QY: Experiment, PW: Analysis; YL: Experiment; JJ: Resources, Supervision; LL: Writing-review & editing, Supervision. All authors read and approved the final manuscript.

Declarations

Conflict of interest The authors declare that they have no conflict of interest.

References

1. Z.A. Chaleshtari, R. Foudazi, ACS Appl. Polym. Mater. **2**, 3196–3204 (2020)
2. Q. Yang, Y. Wang, J. Wang, F. Liu, N. Hu, H. Pei, W. Yang, Z. Li, Y. Suo, J. Wang, Food Chem. **254**, 241–248 (2018)
3. M. Ahmad, M. Yousaf, A. Nasir, I.A. Bhatti, A. Mahmood, X. Fang, X. Jian, K. Kalantar-Zadeh, N. Mahmood, Environ. Sci. Technol. **53**, 2161–2170 (2019)
4. X. Han, Y. Liu, L. Xiong, H. Huang, Q. Zhang, L. Li, X. Yu, L. Wei, Polym. Compos. **40**, E1777–E1785 (2019)
5. J.J. Villora-Picó, V. Belda-Alcázar, M.J. García-Fernández, E. Serrano, A. Sepúlveda-Escribano, M.M. Pastor-Blas, Langmuir **35**, 6089–6105 (2019)
6. M.L. Sall, A.K.D. Diaw, D. Gningue-Sall, A. Chevillot-Biraud, N. Oturan, M.A. Oturan, J.-J. Aaron, Environ. Sci. Pollut. Res. **24**, 21111–21127 (2017)
7. M. Liang, Y.M. Ding, Q. Zhang, D.Q. Wang, H.H. Li, L. Lu, Sci. Rep. **10**, 21473 (2020)
8. Z. Ye, N. Xu, D. Li, J. Qian, C. Du, M. Chen, J. Hazard. Mater. **411**, 125042 (2021)
9. N.S. Marghaki, Z.A. Jonoush, A. Rezaee, J. Clean Prod. **277**, 123195 (2020)
10. Z. Razmara, E. Sanchooli, J. Inorg. Organomet. Polym. **29**, 2090–2102 (2019)
11. J. Bo, X. Luo, H. Huang, L. Li, W. Lai, X. Yu, J. Power Sources **407**, 105–111 (2018)

12. L.M. Santino, Y. Diao, H. Yang, Y. Lu, H. Wang, E. Hwang, J.M. Darcy, Nanoscale **11**, 12358–12369 (2019)
13. D. Wei, J. Zhu, L. Luo, H. Huang, L. Li, X. Yu, J. Mater. Sci. **55**, 11779–11791 (2020)
14. Y.H. Li, L.F. Peng, J. Guo, Z. Chen, Langmuir **36**, 11508–11516 (2020)
15. A. Hosseinkhani, B.F. Rad, M. Baghdadi, J. Environ. Manag. **274**, 111153 (2020)
16. S. Sahu, P. Kar, N. Bishoyi, L. Mallik, R.K. Patel, J. Chem. Eng. Data **64**, 4357–4368 (2019)
17. D. Pakulski, W. Czepa, S. Witomska, A. Aliprandi, P. Pawluc, V. Patroniak, A. Ciesielski, P. Samori, J. Mater. Chem. A **6**, 9384–9390 (2018)
18. N. Wang, X. Li, J. Yang, Y. Shen, J. Qu, S. Hong, Z. Yu, RSC Adv. **6**, 88897–88903 (2016)
19. W.M.A. El Rouby, A.A. Farghali, M.A. Sadek, W.F. Khalil, J. Inorg. Organomet. Polym. **28**, 2336–2349 (2018)
20. S.M. Anush, H.R. Chandan, B.H. Gayathri, N. Asma, B. Manju, B. Vishalakshi, Kalluraya, Int. J. Biol. Macromol. **164**, 4391–4402 (2020)
21. Y. Chen, H. Xu, S. Wang, L. Kang, RSC Adv. **4**, 17805–17811 (2014)
22. W. Yao, T. Ni, S. Chen, H. Li, Y. Lu, Compos. Sci. Technol. **99**, 15–22 (2014)
23. L.L. Fan, C.N. Luo, M. Sun, H.M. Qiu, J. Mater. Chem. **22**, 24577–24583 (2012)
24. X.S. Lv, X.Q. Xue, G.M. Jiang, D.L. Wu, T.T. Sheng, H.Y. Zhou, X.H. Xu, J. Colloid Interface Sci. **417**, 51–59 (2014)
25. J. Ji, X. Zhang, J. Liu, L. Peng, C. Chen, Z. Huang, L. Li, X. Yu, S. Shang, Mater. Sci. Engin. B **198**, 51–56 (2015)
26. W. Zheng, S. Li, X. Yu, C. Chen, H. Huang, Y. Huang, L. Li, Mater. Res. Bull. **80**, 303–308 (2016)
27. L. Tian, M.J. Meziani, F. Lu, C.Y. Kong, L. Cao, T.J. Thorne, Y.-P. Sun, ACS Appl. Mater. Interfaces **2**, 3217–3222 (2010)
28. P. Guo, P. Chen, M. Liu, ACS Appl. Mater. Interfaces **5**, 5336–5345 (2013)
29. X. She, P. Sun, X. Yu, Q. Zhang, Y. Wu, L. Li, Y. Huang, S. Shang, S. Jiang, J. Inorg. Organomet. Polym. **24**, 884–889 (2014)
30. D. Xiao, M. He, Y. Liu, L. Xiong, Q. Zhang, L. Wei, L. Li, X. Yu, Polym. Bull. **77**, 6609–6623 (2020)
31. D. Wei, H. Wang, J. Zhu, L. Luo, H. Huang, L. Li, X. Yu, Macromol. Mater. Eng. **305**, 2000018 (2020)
32. J. Li, X. Yun, Z. Hu, L. Xi, N. Li, H. Tang, P. Lu, Y. Zhu, J. Mater. Chem. A **7**, 26311–26325 (2019)
33. F. Zhang, F. Xiao, Z.H. Dong, W. Shi, Electrochim. Acta **114**, 125–132 (2013)
34. J. Zhang, X. Zhao, J. Phys. Chem. C **116**, 5420–5426 (2012)
35. J. Wu, Y. Wei, H. Ding, Z. Wu, X. Yang, Z. Li, W. Huang, X. Xie, K. Tao, X. Wang, ACS Appl. Mater. Interfaces **12**, 20623–20632 (2020)
36. L. Zhang, W.Y. Niu, J. Sun, Q. Zhou, Chemosphere **248**, 126102 (2020)
37. S. Rafiaee, M.R. Samani, Synth. Met. **265**, 116416 (2020)
38. M. Bhaumik, A. Maity, V.V. Srinivasu, M.S. Onyango, Chem. Eng. J. 181–182, 323 – 33 (2012)
39. T.J. Yao, T.Y. Cui, J. Wu, Q.Z. Chen, S.W. Lu, K.N. Sun, Polym. Chem. **2**, 2893–2899 (2011)
40. R. Karthik, S. Meenakshi, Desalin Water Treat **56**, 1587–1600 (2015)
41. T.C. Maponya, K.E. Ramohlola, N.H. Kera, K.D. Modibane, A. Maity, L.M. Katata-Seru, M.J. Hato, Polymers **12**, 679 (2020)
42. L. Du, P. Gao, Y.L. Liu, T. Minami, C.B. Yu, Nanomater. **10**, 686 (2020)
43. A. Belcaid, B.H. Beakou, K. El Hassani, S. Bouhsina, A. Anouar, Water Sci. Technol. **83**, 556–566 (2021)
44. J. Zhao, L.H. Yu, F. Zhou, H.X. Ma, K.Y. Yang, G. Wu, RSC Adv. **11**, 8025–8032 (2021)
45. M. Bhaumik, A. Maity, V.V. Srinivasu, M.S. Onyango, J. Hazard. Mater. **190**, 381–390 (2011)
46. K. Zhu, Y. Gao, X. Tan, C. Chen, ACS Sustain. Chem. Eng. **4**, 4361–4369 (2016)
47. J. Wang, C. Luo, G. Qi, K. Pan, B. Cao, Appl. Surf. Sci. **316**, 245–250 (2014)

Authors and Affiliations

Song Gao[1,2] · Zhichang Liu[1] · Qunshan Yan[1] · Pei Wei[1] · Yang Li[2] · Jiayou Ji[2] · Liang Li[2]

✉ Jiayou Ji
jijy@wit.edu.cn

✉ Liang Li
msell08@163.com

[1] Key Laboratory of Applied Technology Research of Reconstituted Tobacco of Hubei Province, Hubei Xinye Reconstituted Tobacco Development Co., Ltd, Wuhan 430070, People's Republic of China

[2] Key Laboratory for Green Chemical Process of Ministry of Education, Engineering Research Center of Environmental Materials and Membrane Technology of Hubei Province, Hubei Key Laboratory of Plasma Chemistry and Advanced Materials, School of Materials Science and Engineering, Wuhan Institute of Technology, Wuhan 430205, People's Republic of China